

# Spectral signature of high-order photon processes enhanced by Cooper-pair pairing

Received: 17 July 2024

Accepted: 9 July 2025

Published online: 24 September 2025

Check for updates

W. C. Smith<sup>1,3,4</sup> , A. Borgognoni<sup>1,4</sup>, M. Villiers<sup>1</sup>, E. Roverc'h<sup>1</sup>, J. Palomo<sup>1</sup>, M. R. Delbecq<sup>1</sup> , T. Kontos<sup>1</sup>, P. Campagne-Ibarcq<sup>1</sup> , B. Douçot<sup>2</sup> & Z. Leghtas<sup>1</sup>

Inducing interactions between individual photons is key for photonic quantum information and studying many-body photon states. Superconducting circuits are well suited to combine strong interactions with low losses. Typically, microwave photons are stored in an  $LC$  oscillator shunted by a Josephson junction, where the zero-point phase fluctuations across the junction determine the strength and order of photon interactions. Most superconducting nonlinear oscillators operate with small phase fluctuations, where two-photon Kerr interactions dominate. In our experiment, we shunt a high-impedance  $LC$  oscillator with a dipole element favoring the tunneling of paired Cooper pairs. This leads to large phase fluctuations of 3.4, accessing a regime where transition frequencies shift non-monotonically with excitation number. From spectroscopy, we extract two-, three-, and four-photon interaction energies, all of similar strength and exceeding the photon loss rate. Our results open a new regime of high-order photon interactions in microwave quantum optics.

Photons do not interact with each other in free space. In the quantum optical domain, they are typically brought into interaction by coupling them to atoms<sup>1</sup>. Recent advances have realized two- and three-photon interactions mediated by a dense gas of Rydberg atoms, demonstrating photon dimers and trimers<sup>2</sup>, and photonic vortices<sup>3</sup>. Reaching processes of higher order would find applications in multi-photon quantum logic<sup>4</sup> and the study of many-body photon states<sup>5–7</sup>, but has remained out of reach since it requires inducing even stronger interactions between photons.

In the field of microwave quantum optics with superconducting circuits<sup>8–10</sup>, the nonlinearity of the Josephson junction is employed to mediate interactions between photons. These photons are typically stored in an  $LC$  circuit<sup>11</sup> of angular frequency  $\Omega = 1/\sqrt{LC}$  ( $L$  and  $C$  are the circuit inductance and capacitance, respectively). Superconductivity endows these circuits with low photon loss, and quality factors exceeding one million are routinely observed<sup>12–14</sup>. When such a circuit

is shunted by a Josephson junction, interactions between photons appear (Fig. 1). The Hamiltonian takes the form

$$\hat{\mathcal{H}}_{\text{ideal}} = \hbar\Omega\hat{a}^\dagger\hat{a} - \mathcal{E}_J \cos(\hat{\phi} - \phi_{\text{ext}}) \quad (1)$$

$$\hat{\phi} = \eta(\hat{a} + \hat{a}^\dagger),$$

where  $\hbar$  is the reduced Planck constant and  $\hat{a}$  is the photon annihilation operator. The interaction energy stems from the Josephson cosine potential with Josephson energy  $\mathcal{E}_J$ , and  $\hat{\phi}$  is the phase drop across the junction with  $\eta$  its zero-point fluctuations. The loop formed by the oscillator inductance and the junction is threaded by external magnetic flux denoted  $\phi_{\text{ext}}$ . Expanding the cosine into its Taylor series reveals the various interaction processes. For example, the  $[\eta(\hat{a} + \hat{a}^\dagger)]^4$  term yields a two-photon interaction term  $\hat{a}^{\dagger 2}\hat{a}^2$  corresponding to the Kerr effect. A celebrated success of microwave quantum optics was the

<sup>1</sup>Laboratoire de Physique de l'Ecole Normale Supérieure, ENS-PSL, CNRS, Sorbonne Université, Université Paris Cité, Centre Automatique et Systèmes, Mines Paris, Université PSL, Inria, Paris, France. <sup>2</sup>Laboratoire de Physique Théorique et Hautes Energies, Sorbonne Université and CNRS UMR 7589, 4 place Jussieu, 75252 05 Paris Cedex, France. <sup>3</sup>Present address: Google Quantum AI, Santa Barbara, California, CA, USA. <sup>4</sup>These authors contributed equally: W. C. Smith, A. Borgognoni. ✉e-mail: [smithclarke@google.com](mailto:smithclarke@google.com); [zaki.leghtas@ens.fr](mailto:zaki.leghtas@ens.fr)

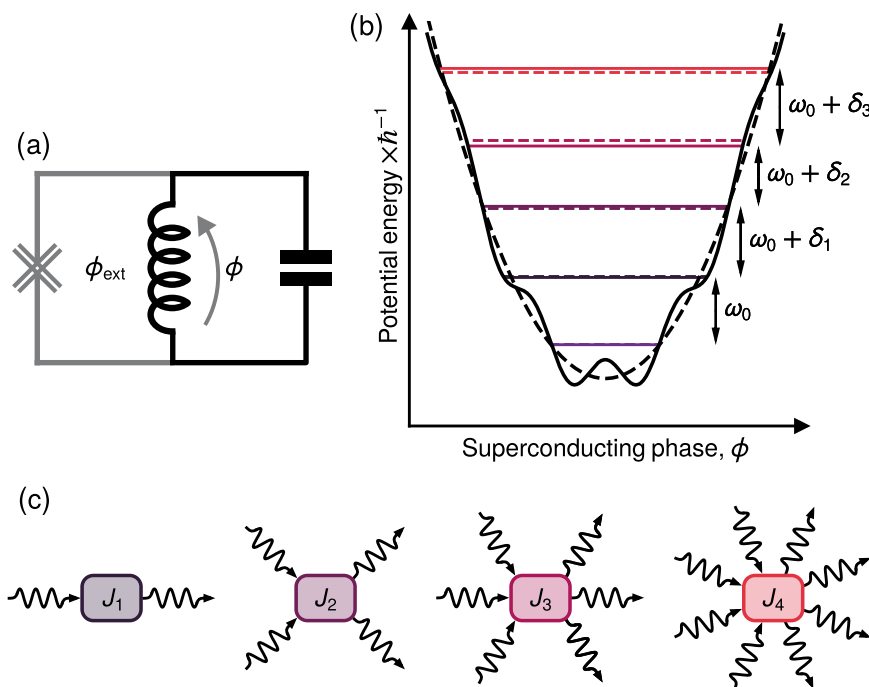


**Fig. 1 | Principle of high-order photon processes.** **a** Electrical circuit depicting a superconducting  $LC$  oscillator (black) shunted by a generalized Josephson junction (grey) that only permits Cooper-pair tunneling in pairs. The circuit is threaded by an external flux denoted  $\phi_{\text{ext}}$ . **b** Potential and energy levels (solid lines) of this non-linear oscillator [Eq. (1) with parameters

$\Omega/2\pi = 2.86$  GHz,  $\mathcal{E}_J/\hbar = 0.795$  GHz,  $\eta = 3.4$ ] and its linear equivalent (dashed lines) as a function of the superconducting phase difference at  $\phi_{\text{ext}} = \pi$ . Crucially, the adjacent transition frequency shift  $\delta_n$  from the bare frequency  $\omega_0$  alternates in sign when ascending the ladder. **c** Photon process diagrams for the first four interaction orders and corresponding interaction energies  $J_n$ .

first realization of a Kerr interaction that exceeded the photon loss rate, demonstrating the collapse of a coherent state into multi-component Schrödinger cat states<sup>15</sup>. In this work, we address the problem of inducing higher-order processes of the form  $\hat{a}^{\dagger n} \hat{a}^n$  where  $n = 3, 4$ , and beyond.

The relative strength of multi-photon processes is governed by the dimensionless quantity  $\eta$ . It can be expressed as  $\eta = \sqrt{LZ/R_Q}$ , where  $Z = \sqrt{L/C}$  is the  $LC$  circuit impedance, and  $R_Q \approx 6.4$  k $\Omega$  is the superconducting resistance quantum<sup>16</sup>. The  $n$ -photon process  $\hat{a}^{\dagger n} \hat{a}^n$  has a strength  $J_n$  that scales as  $(\eta^n/n!)^2$ . Going beyond the Kerr effect requires that  $|J_3/J_2| = \eta/3 \geq 1$ , or equivalently  $Z \gg R_Q$ . However, fabricating an  $LC$  oscillator with a characteristic impedance far exceeding the superconducting resistance quantum is challenging. A successful strategy has been to fabricate the resonator inductance from an array of 40 to 100 Josephson junctions<sup>17,18</sup> or a high kinetic inductance material such as granular aluminum<sup>19</sup>. Values of  $\eta \approx 1.8$  have been achieved, giving rise to the fluxonium qubit. More recently, arrays of 460 Josephson junctions have been suspended above the substrate, achieving  $\eta \approx 3.8$ , and giving rise to the quasicharge qubit<sup>20</sup>. Another strategy has been to fabricate the resonator out of a planar coil of thin superconducting wire. Fluctuations of  $\eta \approx 1$  were achieved, and emissions of  $k$ -photon bunches ( $k = 1$  to 6) were observed by activating the process  $\hat{a}^k + \hat{a}^{\dagger k}$  with a voltage-biased junction<sup>21</sup>. Values as large as  $\eta = 2.4$  were reported by suspending such a planar coil on a thin substrate<sup>22</sup>, leading to the observation of phase delocalization with an uninterrupted wire.

Another route towards large phase fluctuations is to replace the Josephson junction, that allows Cooper-pair tunneling, by a dipole that only allows pairs of Cooper pairs to tunnel<sup>23,24</sup>. In the basis of tunneled Cooper-pair number  $N$ , the tunneling operator is transformed as  $\frac{1}{2} \sum_N (|N\rangle \langle N+1| + |N+1\rangle \langle N|) \rightarrow \frac{1}{2} \sum_N (|N\rangle \langle N+2| + |N+2\rangle \langle N|)$ .

Equivalently, in the conjugate phase representation  $\varphi$ ,  $\cos \hat{\varphi} \rightarrow \cos 2\hat{\varphi}$ . Shunting such an element by an  $LC$  oscillator (Fig. 1a), and denoting  $\hat{\varphi} = 2 \times \hat{\phi}$ , we see that phase fluctuations are effectively doubled:  $\eta = 2 \times \sqrt{\pi Z/R_Q}$ <sup>25</sup>. In the extreme regime of  $\eta \gtrsim 3$ , we further require that  $\mathcal{E}_J \ll \hbar\Omega$  (Fig. 1b), so that the Josephson cosine potential primarily induces  $n$ -photon interaction processes  $\hat{a}^{\dagger n} \hat{a}^n$  (Fig. 1c).

In this experiment, we implement a superconducting  $LC$  oscillator shunted by an approximate two-Cooper-pair tunneling element. We place ourselves in the unexplored regime where the tunneling energy is smaller than the oscillator transition energies, and photon-photon interactions of order larger than two (Kerr) dominate, or equivalently zero-point phase fluctuations exceed 3. We achieve  $\mathcal{E}_J/\hbar\Omega = 0.28$  and  $\eta = 3.4$ . We probe our circuit through microwave spectroscopy, which is better suited than correlation measurements to the regime where interactions exceed the oscillator linewidth. We measure the first four transition energies of our device, and find that unlike a Kerr resonator, they do not follow a monotonic trend. Instead, we observe an alternation of the sign of the oscillator frequency shift for each added photon. From this spectroscopic signature, we extract two-, three-, and four-photon interaction processes of amplitudes greater than 70 MHz, that alternate in sign, and far exceed the transition linewidths of 200 kHz. Entering the regime of strong high-order photon interactions opens many possibilities in microwave quantum optics such as multi-photon quantum logic<sup>4</sup>, the study of many-body photon states<sup>6</sup>, or the processing of protected qubits<sup>26</sup>.

## Results

We proceed to the analysis of the ideal Hamiltonian in Eq. (1) in the regime  $\mathcal{E}_J \ll \hbar\Omega$  and  $\eta > 1$  (Fig. 1), and for simplicity, we set  $\phi_{\text{ext}} = 0$ . Note that the cosine in Eq. (1) may be decomposed as  $\cos[\eta(\hat{a} + \hat{a}^\dagger)]$

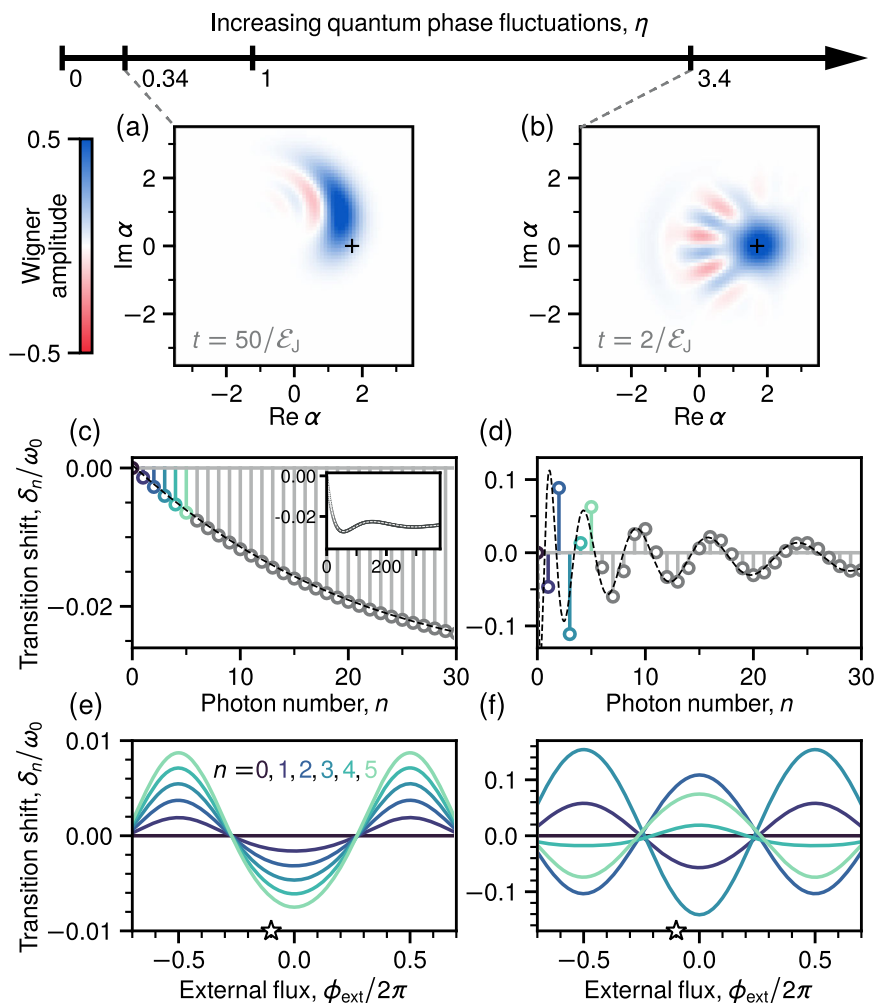


**Fig. 2 | Signatures of higher-order photon processes.** **a, b** Simulated Wigner quasiprobability distribution representing the initial time evolution of the coherent state  $|\alpha\rangle$  with  $\alpha = 1.7$  for small and large quantum phase fluctuations. This value of  $\alpha$  was chosen to match  $\eta/2$  for  $\eta = 3.4$  (see text). As quantum phase fluctuations increase, the evolution remarkably transitions from diffusive to nondiffusive. **c–f** Simulated transition frequency shifts  $\delta_n = \omega_n - \omega_0$ , where  $\omega_n$  is the transition frequency between

energy levels  $n$  and  $n + 1$ , represented versus photon number at the starred external flux value (**c, d**), and versus external flux (**e, f**). We observe the transition from an ordered to an alternating arrangement that asymptotically approaches a Bessel function (dashed lines). Simulations correspond to numerical diagonalization and time propagation of Eq. (1) with parameters  $\Omega/2\pi = 2.86$  GHz,  $\varepsilon_J/\hbar = 0.795$  GHz and  $\eta = 0.34$  for (**a**), (**c**), (**e**) and  $\eta = 3.4$  for (**b**), (**d**), (**f**) as indicated by the top axis.

$= \frac{1}{2}(\hat{D}_\eta + \hat{D}_{-\eta})$ , where  $\hat{D}_\eta = \exp[i\eta(\hat{a} + \hat{a}^\dagger)]$  is the displacement evolution operator. Remarkably, this evolution operator that usually results from the integration of a linear Hamiltonian  $\propto \hat{a} + \hat{a}^\dagger$  over time enters the Hamiltonian directly. As a consequence, even at short times, a quantum state evolving under the Hamiltonian in Eq. (1) will be displaced across phase-space by  $\pm \eta$ . The effect is particularly striking when initializing the system in a coherent state of amplitude  $\alpha = \eta/2^{26}$ , so that  $|\pm\alpha\rangle$ , that are distant by  $2\alpha$  in phase-space, are directly coupled through  $\cos[\eta(\hat{a} + \hat{a}^\dagger)]$  (Fig. 2b). This is qualitatively different from the familiar diffusive-like evolutions resulting from low-order photon interactions<sup>15</sup> (Fig. 2a).

We now express  $\hat{\mathcal{H}}_{\text{ideal}}$  in Eq. (1) in terms of  $n$ -photon interaction processes (Fig. 1c). We start by expanding the cosine into a normal ordered Taylor expansion. Since  $\varepsilon_J \ll \hbar\Omega$ , by virtue of the rotating wave approximation (RWA), we neglect non-particle number conserving terms. We arrive at (see Supplementary Information):

$$\hat{\mathcal{H}}_{\text{ideal}} \approx \hbar\omega_0 \hat{a}^\dagger \hat{a} + \sum_{n \geq 2} J_n \hat{a}^{\dagger n} \hat{a}^n, \quad (2)$$

where the  $n$ -photon interaction energy takes the form  $J_n = -\varepsilon_J e^{-\eta^2/2} (-1)^n (\eta^n/n!)^2$ , and the renormalized frequency is  $\omega_0 = \Omega + J_1/\hbar$ .

Note that  $J_n/J_{n-1} = -(\eta/n)^2$ , and hence the interaction strength is maximal for the integer order closest to  $\eta$ . The eigenstates of Hamiltonian (2) are Fock states with eigenenergies  $E_n = n\hbar\omega_0 + \sum_{k=2}^n \frac{n!}{(n-k)!} J_k$ , and the experimentally accessible quantities are the transition frequencies  $\omega_n = (E_{n+1} - E_n)/\hbar$ . We introduce the transition frequency shift in the presence of  $n$  photons as  $\delta_n = \omega_n - \omega_0$  (Fig. 1b) and we find:

$$\delta_n = \sum_{k=2}^{n+1} k \frac{n!}{(n+1-k)!} J_k/\hbar. \quad (3)$$

In the familiar situation of the Kerr oscillator where  $\eta \ll 1$ ,  $J_2 \approx -\varepsilon_J \eta^4/4$  is half the Kerr shift per photon and  $J_{n \geq 3}$  can be neglected. Hence  $\omega_n \approx \omega_0 + 2nJ_2/\hbar$  and the transition frequency monotonically shifts for each added photon (Fig. 2c, e). This is in stark contrast with the regime of extreme phase fluctuations explored in this work where the transition frequency shift may alternate in sign for each added photon (Fig. 2d, f). This resembles the oscillatory nonlinearity predicted in a resonator containing a phase-slip element<sup>27</sup>.

Our circuit implementation of  $\hat{\mathcal{H}}_{\text{ideal}}$  in Eq. (1) is depicted in Fig. 3a, b. It consists of a high impedance LC oscillator. The inductance, which we aim to maximize, is formed by a chain of 109

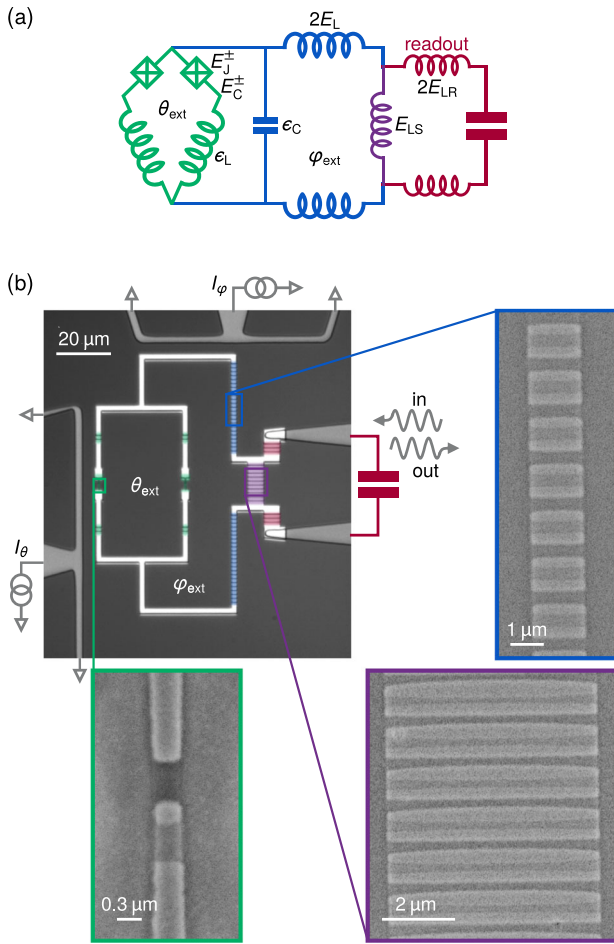


**Fig. 3 | Experimental implementation.** **a** Lumped element circuit of the LC oscillator (blue) shunted by the KITE (green) and coupled through a shared inductance (purple) to a readout mode (red). The two small junctions have slightly different Josephson energies  $E_J^\pm = (1 \pm \epsilon)E_J$  and charging energies  $E_C^\pm = E_C/(1 \pm \epsilon)$ , with  $\epsilon \ll 1$ , due to junction fabrication variation. **b** Optical micrograph of the physical device, with false color indicating the constituent Josephson junctions and their respective scanning electron microscope images (from a nominally identical sample). Aluminum and niobium electrodes appear in white and grey, respectively. (Green frame) one of the two small KITE junctions. (Blue frame) 14 of the array junctions that form both the internal KITE inductance and the inductive shunt. (Purple frame) 12 of the array junctions that form the shared inductance between the circuit and the readout resonator, as well as the self-inductance of the readout. All junctions are fabricated in one step using Dolan bridges.

Josephson junctions, 19 of which are shared with a readout resonator (inductive energy  $E_{LS}/h = 11.91$  GHz) and 90 unshared junctions (inductive energy  $E_L/h = 0.57$  GHz). Note that approximating the junction chain inductance by a single inductor is only valid at frequencies lower than the first chain mode (that we estimate above 10 GHz). The capacitance, which we aim to minimize, has multiple contributions. The first one is the self capacitances of the small junctions in the tunneling element (described below) attached to the chain of junctions. The second one arises from the capacitance between the two wires linking the chain of junctions to the tunneling element, resulting in a charging energy  $\epsilon_C/h = 3.24$  GHz (estimated from finite-element simulations). Other sources of capacitive loading, not accounted for in our model, are from the self capacitance and capacitance to ground of the chain junctions<sup>28</sup>.

Tunneling occurs through a so-called Kinetic Interference coTunneling Element (KITE)<sup>25,29</sup>. It consists of two parallel arms that form a loop threaded by an external flux  $\theta_{ext}$ . Each arm contains a small junction of Josephson energy  $E_J^\pm = E_J(1 \pm \epsilon)$  and charging energy

$E_C^\pm = E_C/(1 \pm \epsilon)$ , with  $E_J/h = 3.98$  GHz,  $E_C/h = 10.40$  GHz and fabrication uncertainty results in a small asymmetry factor  $\epsilon = 0.033$ . Each small junction is placed in series with 6 large junctions of a total inductive energy  $\epsilon_L/h = 6.16$  GHz. Additionally, our chip contains a lumped LC readout resonator composed of two planar capacitor pads (not shown in Fig. 3b) and an array of 29 junctions, 19 of which are shared with the main circuit, and 10 unshared junctions (inductive energy  $E_{LR}/h = 18.03$  GHz). Through the small KITE junctions, this inductive coupling induces a dispersive interaction between the circuit and its readout resonator<sup>30</sup>. Finally, our circuit hosts a “parasitic” mode, visible in electromagnetic simulations, where current flows symmetrically through both halves of the junction chain (with minimal current in the shared junctions), charging and discharging a capacitor (not represented in Fig. 3a) formed between the readout pads and the connecting leads to the KITE.

The circuit parameters quoted above are extracted by fitting a five-mode circuit model (see Supplementary Information) (including the readout and parasitic modes) to two-tone spectroscopy data at various flux biases ( $\theta_{ext}$ ,  $\varphi_{ext}$ ) (Fig. 4a–d). This five-mode Hamiltonian is  $2\pi$  periodic in ( $\theta_{ext}$ ,  $\varphi_{ext}$ ) and its spectrum possesses inversion symmetry about  $(\theta_{ext}, \varphi_{ext}) = (0, 0)$ ,  $(0, \pi)$ ,  $(\pi, 0)$ , and  $(\pi, \pi)$ <sup>31</sup>. Therefore, these four points are the vertices of a plaquette that constitutes the primitive cell of the circuit spectrum as a function of external flux. We acquire the circuit spectrum along the edges of this plaquette [diagrams in Fig. 4a–d]. At each bias point, we start by acquiring the reflection spectrum of the readout resonator (Fig. 4e–h). We then set the readout tone on resonance, and sweep a probe tone over a broad spectral range (Fig. 4a–d). When the probe hits a circuit transition from the low lying states to the  $n$ -th excited state, the reflected readout signal is affected. We identify several transitions that are captured by a five-mode circuit model (see Supplementary Information) (semi-transparent lines). The features near 5.1 GHz and 4.4 GHz correspond to the readout and parasitic modes, respectively. The circuit parameters we extract from this fit are summarized in Table 1.

We now delve into explaining how our circuit emulates the Hamiltonian of Eq. (1). Here, we will provide an intuitive understanding of this circuit, and refer the reader to the appendices for a more rigorous analysis. We start by discarding the readout mode, the parasitic mode, and the two KITE self-resonant high-frequency modes, and focus on the LC oscillator. Since  $E_{LS} \gg E_L$ , the total oscillator inductive energy is approximately  $E_L$ . The total oscillator charging energy is  $\epsilon_{C,tot} = 1/(2/E_C + 1/\epsilon_C) = h \times 2.0$  GHz. The resonant frequency of this oscillator is  $\Omega \approx \sqrt{8E_L\epsilon_{C,tot}}/\hbar$ . In the regime  $\epsilon_L \gg E_J$ , the potential energy of one arm of the KITE traversed by a phase drop of  $\varphi$  takes the form  $U^\pm(\varphi) \approx$

$-E_J^\pm \cos \varphi + \frac{E_J^2}{4\epsilon_L} \cos 2\varphi$  and higher harmonics have been neglected (see Supplementary Information). Biasing the circuit at  $\theta_{ext} = 0$ , both Cooper-pair tunneling and cotunneling across both arms interfere constructively. Indeed, the potential energy of the KITE is  $U^+(\varphi) + U^-(\varphi) \approx -2E_J \cos \varphi + \frac{E_J^2}{2\epsilon_L} \cos 2\varphi$ . Biasing the circuit at  $\theta_{ext} = \pi$ , Cooper-pair tunneling across both arms interferes destructively, while cotunneling interferes constructively. Indeed, the potential energy of the KITE is  $U^+(\varphi) + U^-(\varphi + \pi) \approx -2\epsilon E_J \cos \varphi + \frac{E_J^2}{2\epsilon_L} \cos 2\varphi$ . In summary, this yields an effective Hamiltonian for our circuit of the form (see Supplementary Information):

$$\hat{\mathcal{H}}_{\text{circuit}}(\theta_{ext}) = \hbar \Omega \hat{a}^\dagger \hat{a} - E_{J1}(\theta_{ext}) \cos(\hat{\varphi} - \varphi_{ext}) + E_{J2} \cos[2(\hat{\varphi} - \varphi_{ext})], \quad (4)$$

where  $\varphi_{ext}$  is the flux threading the loop formed by the KITE and the oscillator inductance and the phase operator verifies  $\hat{\varphi} = \varphi_{zpf}(\hat{a} + \hat{a}^\dagger)$ , where  $\varphi_{zpf} = (2\epsilon_{C,tot}/E_L)^{1/4}$  is the zero-point phase fluctuations.



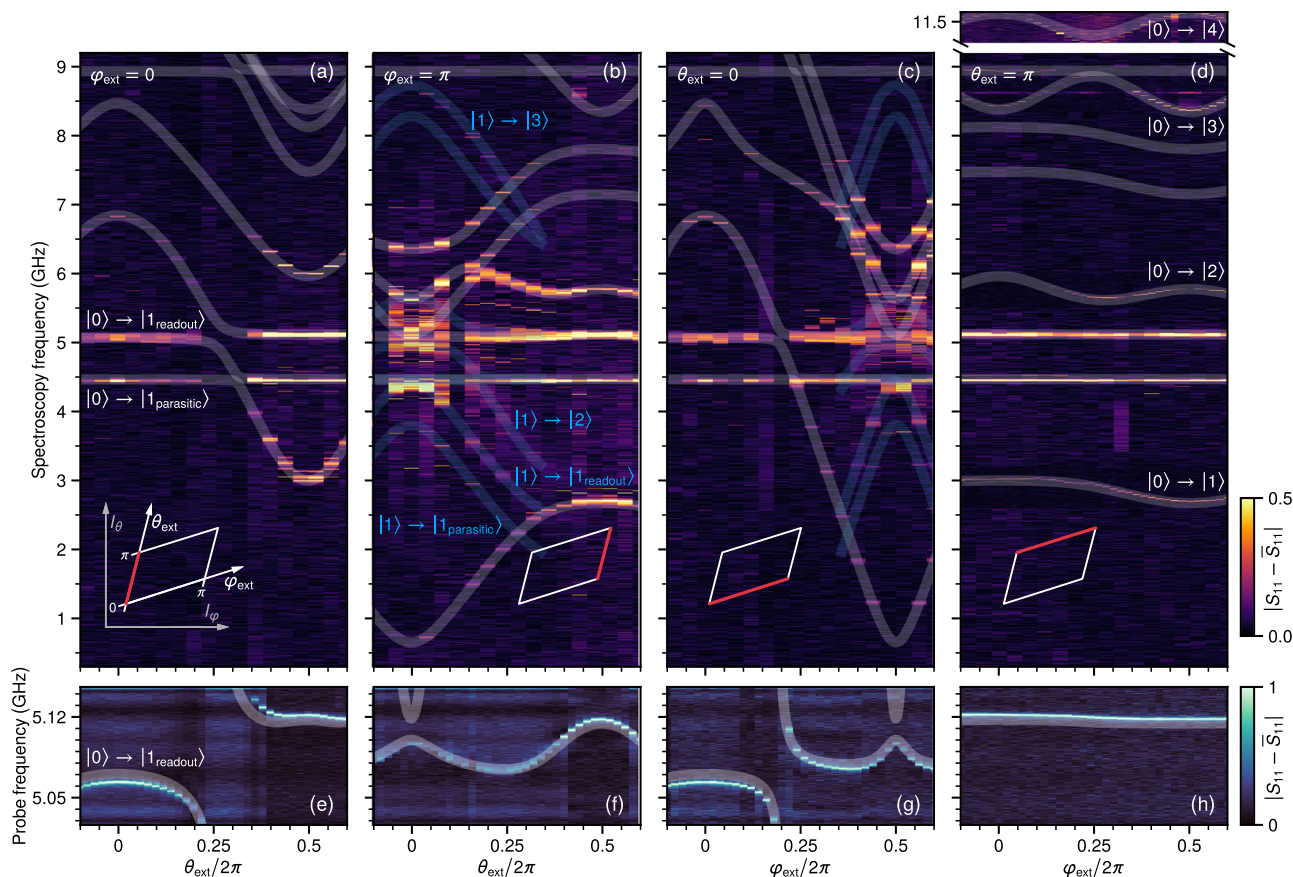


**Fig. 4 | Spectroscopy measurements.** **a–d** Two-tone reflection spectroscopy (background subtracted) of the lowest transitions of the circuit along the four edges of the primitive cell in the two-dimensional external flux landscape (inset diagrams), and **(e–h)** accompanying readout spectroscopy. Theoretical transition frequencies from the ground state (semi-transparent white lines) are obtained from numerical diagonalization of the five-mode circuit model with seven fitted

Hamiltonian parameters (see Table 1). Additionally, transition frequencies from the first excited state (semi-transparent blue lines) are shown when the first excited state has a transition frequency that falls below 2.5 GHz and is therefore thermally occupied. Note that this model includes the nearly harmonic readout and parasitic modes [labeled in **(a)**]. Scans around the  $|0\rangle \rightarrow |n\rangle$  transitions for  $n = 1 - 4$  [labeled in **(d)**] are enlarged in Fig. S8.

**Table 1 | Device parameters corresponding to the five-mode circuit in Fig. 3a**

$E_J/h$	$E_C/h$	$E_L/h$	$\epsilon_L/h$	$\epsilon$	$E_{LR}/h$	$E_{LS}/h$	$\epsilon_C/h$
3.98	10.40	0.57	6.16	0.033	18.03	11.91	3.24

The first seven parameters are found by fitting the spectral lines in Fig. 4a–h to the circuit Hamiltonian, with all capacitances (except junction capacitances) fixed to values from finite-element simulations (see Supplementary Information). The final parameter—the oscillator charging energy in the absence of the junctions—is computed from the full device capacitance matrix and is not found from the fit.

Let us now analyze the case where  $\theta_{\text{ext}} = 0$  (Fig. 5a, c). From the simple theory sketched above, we expect  $E_J(\theta_{\text{ext}} = 0) \approx 2E_J$  and  $E_{J2}(\theta_{\text{ext}} = 0) \approx E_J^2/2\epsilon_L$ . In the regime of this experiment where  $E_J \ll \epsilon_L$ , we have  $E_{J2} \ll E_J$ , and so the dominant term in the potential is the regular Cooper-pair tunneling energy. Recall that the term in  $\Omega \hat{a}^\dagger \hat{a}$  may be equivalently recast as  $4\epsilon_{C,\text{tot}} \hat{N}^2 + \frac{1}{2} E_L \hat{\phi}^2$ , where  $\hat{N}$  is the Cooper-pair number operator conjugate to  $\hat{\phi}$ . Interestingly, our experiment is in the regime where  $E_J \gtrsim \epsilon_{C,\text{tot}} \gg E_L$ , which is typical of a fluxonium<sup>17</sup>. The fluxonium is nothing like an anharmonic oscillator. Indeed, the fluxonium eigenstates include fluxon states pinned in Josephson wells (Fig. 5a), and that therefore strongly disperse with flux (Fig. 5c), and plasmon states that are weakly flux-dependent. An anharmonic oscillator only has weakly flux-sensitive plasmon states. Consequently, the language of interacting photons is not adapted to describe a fluxonium.

We now turn to the case where  $\theta_{\text{ext}} = \pi$  (Fig. 5b, d). From the simple theory sketched above, we expect  $E_J(\theta_{\text{ext}} = \pi) \approx 2\epsilon_L$  and

$E_{J2}(\theta_{\text{ext}} = \pi) \approx E_J^2/2\epsilon_L$ . Conveniently, for sufficiently symmetrical junctions and adequately choosing  $E_J \ll \epsilon_L$ , we may enter the regime where  $E_J \ll E_{J2} \ll \Omega$ . In this regime, the potential is dominated by Cooper-pair cotunneling, while regular tunneling may be considered an undesired perturbation. In addition, these nonlinear terms are smaller than the linear oscillator term  $\Omega \hat{a}^\dagger \hat{a}$ . Consequently, this system is well described by a nonlinear oscillator of quasi-equally spaced photonic Fock states that couple through Cooper-pair cotunneling (Fig. 5b, d). The extent of the zero-point phase fluctuations is visible through the number of Josephson corrugations covered by the ground state wave-function. We may now establish a correspondence with the ideal Hamiltonian of Eq. (1). Note that  $\hat{H}_{\text{circuit}}(\theta_{\text{ext}} = \pi)$  corresponds to  $\hat{H}_{\text{ideal}}$  up to the perturbative term in  $E_J$ , with the correspondence  $\epsilon_J = E_{J2}$ ,  $\hat{\phi} = 2\hat{\varphi}$  and hence  $\eta = 2 \times \varphi_{\text{zpf}}$  and  $\phi_{\text{ext}} = 2\varphi_{\text{ext}} + \pi$ . Additionally, the  $J_n$  obtained from Eq. (4) depend on external flux and contain an added contribution from the term in  $E_J$ .

The ability to switch our device in-situ from a familiar fluxonium-like circuit to an original nonlinear oscillator endowed with high-order interactions is convenient to benchmark our system. We extract the parameters of the one-mode Hamiltonian in Eq. (4) by fitting this model to the measured  $\varphi_{\text{ext}}$ -dependent transition energies at  $\theta_{\text{ext}} = 0$  and  $\pi$  (Fig. 5). The resulting parameters are displayed in Table 2. For each  $\varphi_{\text{ext}}$ -dependent dataset, we perform a four-parameter fit ( $\Omega, E_J, E_{J2}, \varphi_{\text{zpf}}$ ). The fits converge on two values of  $\Omega$  that are within 3% of each other,  $E_{J2}$  within 20% and  $\varphi_{\text{zpf}}$  within 2%. This is consistent with the prediction that these parameters should be the same at  $\theta_{\text{ext}} = 0$  and

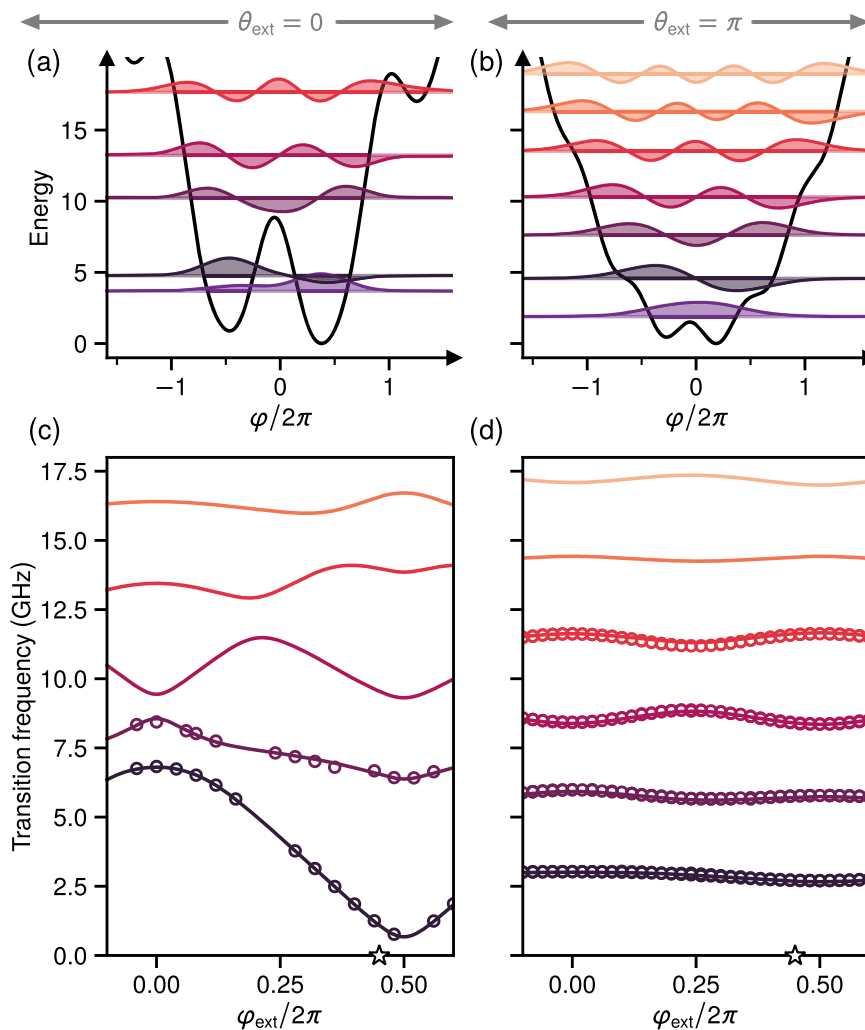


**Fig. 5 | Switching our circuit between a fluxonium and an oscillator with high order interactions. a, b** Potential energy  $U(\varphi) = \frac{1}{2}E_L\varphi^2 - E_J\cos(\varphi - \varphi_{\text{ext}}) + E_J\cos[2(\varphi - \varphi_{\text{ext}})]$  as a function of superconducting phase at  $\varphi_{\text{ext}} = 0.9\pi$  [starred in (c, d)], for (a)  $\theta_{\text{ext}} = 0$  and (b)  $\theta_{\text{ext}} = \pi$ . **c, d** Transition frequencies from the ground

state as a function of external flux. The data points (open circles) correspond to the average of resonances visible in scans such as Fig. 4(c, d). Theoretical transition energies (solid lines) are obtained from Hamiltonian (4) with fitted parameters reported in Table 2.

**Table 2 | Extracted one-mode model parameters found by fitting the measured transition frequencies at  $\theta_{\text{ext}} = 0, \pi$  (Fig. 5) to the effective one-mode Hamiltonian in Eq. (4)**

$\theta_{\text{ext}}$	$\Omega/2\pi$	$E_J/h$	$E_J/h$	$\Phi_{\text{zpf}}$	$2\Phi_{\text{zpf}}$
0	2.95	5.31	0.658	1.67	3.34
$\pi$	2.86	0.27	0.795	1.70	3.40

All energy scales are given in gigahertz.

$\pi$ . On the other hand, the fit converges on two very different values for  $E_J$ . Indeed, its value at  $\theta_{\text{ext}} = \pi$  is 20 times smaller than the one at  $\theta_{\text{ext}} = 0$ . This is consistent with our understanding that regular Cooper-pair tunneling constructively interferes at  $\theta_{\text{ext}} = 0$ , while it destructively interferes at  $\theta_{\text{ext}} = \pi$ .

Finally, we focus on the case  $\theta_{\text{ext}} = \pi$  in order to extract multi-photon interaction strengths from the measured transition frequencies (Fig. 6). Two notable features are visible in the data. First, as previously discussed, these transition frequencies vary in a  $\pm 500\text{MHz}$  window—a  $\pm 17\%$  fraction of the central frequency  $\Omega/2\pi = 2.86\text{GHz}$ . This confirms that the flux-dependent tunneling amplitude is a perturbation to the  $LC$  oscillator frequency, i.e.  $E_J, E_J < \hbar\Omega$ . In particular, we find  $E_J/h = 0.795\text{GHz}$  and the perturbation  $E_J/h = 0.27\text{GHz}$ . Second, the transition frequencies  $\omega_n$

between levels  $n$  and  $n+1$  are not ordered in  $n$ . Instead, they interlace as a function of  $\varphi_{\text{ext}}$ , indicating that we have entered the regime of large phase fluctuations. For example, at  $\varphi_{\text{ext}}/2\pi = 0.2$ ,  $\omega_0 > \omega_1$ ,  $\omega_1 < \omega_2$ , and  $\omega_2 > \omega_3$  (Fig. 6b). From this measured spectrum, we compute the  $n$ -photon interaction strengths  $J_n$  for  $n = 2, 3$ , and 4 (Fig. 6c) by inverting Eq. (3). Notice that  $J_1$  is experimentally inaccessible since it corresponds to the shift between the measured transition frequency  $\omega_0$  and the  $LC$  resonance  $\Omega$  in the absence of the tunneling element. Notably, we find that  $|J_2| \approx |J_3|$ , which is consistent with the extracted  $2\Phi_{\text{zpf}} = 3.4$ .

## Discussion

In conclusion, this experiment explores a new regime of nonlinear microwave quantum optics where interactions between photons are so strong that second-, third-, and fourth-order processes are of comparable amplitude and largely exceed the photon decay rate. We access this regime with photons stored in a high impedance  $LC$  oscillator that is shunted by a two-Cooper-pair tunneling element, effectively boosting phase fluctuations. Two technical challenges must be met: the tunneling energy  $E_J$  must be weaker than the oscillator energy  $\hbar\Omega$ , and the boosted phase fluctuations  $2\Phi_{\text{zpf}}$  across the tunneling element must exceed 3. We measure the first four transition frequencies of our circuit, and observe their interlacing

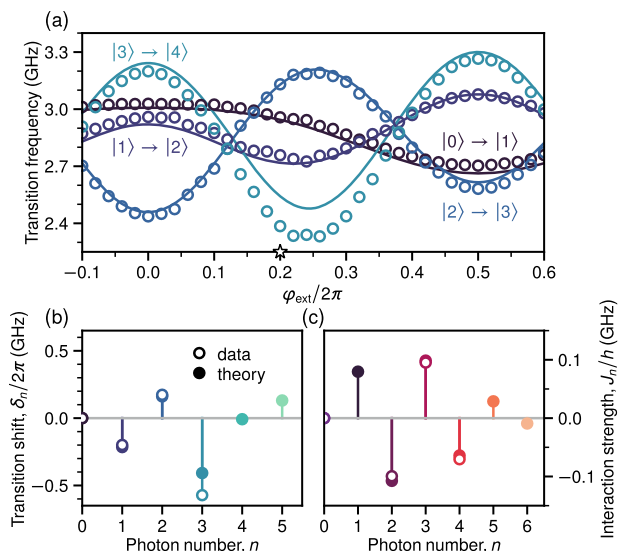


**Fig. 6 | Spectral interlacing.** **a** Adjacent transition frequencies obtained from two-tone measurements (open circles) and numerical diagonalization of the one-mode Hamiltonian of Eq. (4) (solid curves) along  $\theta_{\text{ext}} = \pi$ . **b** Transition frequency shifts  $\delta_n$  and **c** interaction strengths  $J_n$  extracted from measurements (open circles) and analytic expressions depending on the fitted circuit parameters (full circles) at the starred external flux value. The transition frequency shifts alternate in sign while remaining much smaller than the transition frequency itself, directly corresponding to similarly-sized Hamiltonian coefficients for two-, three-, and four-photon interaction strengths.

versus flux. From these spectra, we extract  $E_J/\hbar\Omega = 0.28$  and  $2\varphi_{\text{zpf}} = 3.4$ .

This experiment could be extended in multiple ways. First, one could improve the quantitative analysis by improving the spectroscopic data (larger frequency spans, denser flux sweeps and more averaging). Another direction could be the study of the quantum dynamics and scattered radiation correlations of this system under the action of drives and dissipation<sup>27</sup>. Moreover, coupling our two-Cooper-pair tunneling element to an array of resonators could induce high-order interactions between multiple modes, useful for the study of many-body photon states<sup>5,6</sup>. Finally, applications are envisioned to process quantum information that is encoded non-locally over the phase space of an oscillator<sup>26</sup>.

## Data availability

The data that support the findings of this work are available from the corresponding author upon request.

## Code availability

The code used for data acquisition, analysis and visualization is available from the corresponding author upon request.

## References

- Chang, D. E., Vuletić, V. & Lukin, M. D. Quantum nonlinear optics—photon by photon. *Nat. Photonics* **8**, 685 (2014).
- Liang, Q.-Y. et al. Observation of three-photon bound states in a quantum nonlinear medium. *Science* **359**, 783 (2018).
- Drori, L. et al. Quantum vortices of strongly interacting photons. *Science* **381**, 193 (2023).
- Adhikari, P., Hafezi, M. & Taylor, J. M. Nonlinear optics quantum computing with circuit QED. *Phys. Rev. Lett.* **110**, 060503 (2013).
- Greentree, A. D., Tahan, C., Cole, J. H. & Hollenberg, L. C. L. Quantum phase transitions of light. *Nat. Phys.* **2**, 856–861 (2006).
- Ma, R. et al. A dissipatively stabilized Mott insulator of photons. *Nature* **566**, 51–57 (2019).
- Carusotto, I. et al. Photonic materials in circuit quantum electrodynamics. *Nat. Phys.* **16**, 268–279 (2020).
- Wallraff, A. et al. Strong coupling of a single photon to a superconducting qubit using circuit quantum electrodynamics. *Nature* **431**, 162 (2004).
- Hofheinz, M. et al. Synthesizing arbitrary quantum states in a superconducting resonator. *Nature* **459**, 546 (2009).
- Lang, C. et al. Correlations, indistinguishability and entanglement in Hong–Ou–Mandel experiments at microwave frequencies. *Nat. Phys.* **9**, 345 (2013).
- Devoret, M. H. Quantum fluctuations in electrical circuits, in *Quantum Fluctuations (Les Houches Session LXIII)*, edited by Reynaud, S., Giacobino, E. and Zinn-Justin, J. pp. 351–386 (North-Holland, 1997).
- Place, A. P. M. et al. New material platform for superconducting transmon qubits with coherence times exceeding 0.3 milliseconds. *Nat. Commun.* **12**, <https://doi.org/10.1038/s41467-021-22030-5> (2021).
- Ganjam, S. et al. Surpassing millisecond coherence times in on-chip superconducting quantum memories by optimizing materials, processes, and circuit design, arXiv:2308.15539 (2023).
- Kono, S. et al. Mechanically induced correlated errors on superconducting qubits with relaxation times exceeding 0.4 milliseconds, arXiv:2305.02591 (2023).
- Kirchmair, G. et al. Observation of quantum state collapse and revival due to the single-photon Kerr effect. *Nature* **495**, 205 (2013).
- Girvin, S. M. Circuit QED: Superconducting qubits coupled to microwave photons, in *Quantum Machines: Measurement and Control of Engineered Quantum Systems (Les Houches Session XCVI)*, edited by Devoret, M., Huard, B., Schoelkopf, R., and Cugliandolo, L. F. pp. 113–256 (Oxford University Press, 2014).
- Manucharyan, V. E., Koch, J., Glazman, L. I. & Devoret, M. H. Fluxonium: Single Cooper-pair circuit free of charge offsets. *Science* **326**, 113 (2009).
- Pop, I. M. et al. Coherent suppression of electromagnetic dissipation due to superconducting quasiparticles. *Nature* **508**, 369 (2014).
- Grünhaupt, L. et al. Granular aluminium as a superconducting material for high-impedance quantum circuits. *Nat. Mater.* **18**, 816 (2019).
- Pechenezhskiy, I. V., Mencia, R. A., Nguyen, L. B., Lin, Y.-H. & Manucharyan, V. E. The superconducting quasicharge qubit. *Nature* **585**, 368 (2020).
- Ménard, G. C. et al. Emission of photon multiplets by a dc-biased superconducting circuit. *Phys. Rev. X* **12**, 021006 (2022).
- Peruzzo, M. et al. Geometric superinductance qubits: Controlling phase delocalization across a single Josephson junction. *PRX Quantum* **2**, 040341 (2021).
- Douçot, B. & Vidal, J. Pairing of Cooper pairs in a fully frustrated Josephson-junction chain. *Phys. Rev. Lett.* **88**, 227005 (2002).
- Ioffe, L. B. & Feigel'man, M. V. Possible realization of an ideal quantum computer in Josephson junction array. *Phys. Rev. B* **66**, 224503 (2002).
- Smith, W. C., Kou, A., Xiao, X., Vool, U. & Devoret, M. H. Superconducting circuit protected by two-Cooper-pair tunneling. *npj Quantum Inf.* **6**, 8 (2020).
- Cohen, J., Smith, W. C., Devoret, M. H. & Mirrahimi, M. Degeneracy-preserving quantum nondemolition measurement of parity-type observables for cat qubits. *Phys. Rev. Lett.* **119**, 060503 (2017).
- Hriscu, A. M. & Nazarov, Y. V. Model of a proposed superconducting phase slip oscillator: A method for obtaining few-photon nonlinearities. *Phys. Rev. Lett.* **106**, 077004 (2011).
- Viola, G. & Catelani, G. Collective modes in the fluxonium qubit. *Phys. Rev. B* **92**, 224511 (2015).
- Bell, M. T., Paramanandam, J., Ioffe, L. B. & Gershenson, M. E. Protected Josephson rhombus chains. *Phys. Rev. Lett.* **112**, 167001 (2014).

30. Smith, W. C. et al. Quantization of inductively shunted superconducting circuits. *Phys. Rev. B* **94**, 144507 (2016).
31. Smith, W. C. et al. Magnifying quantum phase fluctuations with Cooper-pair pairing. *Phys. Rev. X* **12**, 021002 (2022).

## Acknowledgements

W.C.S. acknowledges fruitful discussions with Agustin Di Paolo. The devices were fabricated within the consortium Salle Blanche Paris Centre. We thank Jean-Loup Smirre and the Collège de France for providing nano-fabrication facilities. This work was supported by the QuantERA grant QuCOS, by ANR 19-QUAN-0006-04. This project has received funding from the European Research Council (ERC) under the European Union's Horizon 2020 research and innovation program (grant agreement no. 851740). This work has been funded by the French grants ANR-22-PETQ-0003 and ANR-22-PETQ-0006 under the "France 2030 Plan."

## Author contributions

W.C.S. and Z.L. conceived the experiment. W.C.S. and A.B. designed and measured the device. A.B. fabricated the sample. W.C.S., A.B. and Z.L. analyzed the data. M.V., J.P., M.R.D., T.K. and P.C-I. provided experimental support. E.R. and B.D. provided theory support. W.C.S., A.B. and Z.L. co-wrote the manuscript with input from all authors.

## Competing interests

The authors declare no competing interests.

## Additional information

**Supplementary information** The online version contains supplementary material available at <https://doi.org/10.1038/s41467-025-62047-8>.

**Correspondence** and requests for materials should be addressed to W. C. Smith or Z. Leghtas.

**Peer review information** : *Nature Communications* thanks the anonymous reviewers for their contribution to the peer review of this work. A peer review file is available.

**Reprints and permissions information** is available at <http://www.nature.com/reprints>

**Publisher's note** Springer Nature remains neutral with regard to jurisdictional claims in published maps and institutional affiliations.

**Open Access** This article is licensed under a Creative Commons Attribution-NonCommercial-NoDerivatives 4.0 International License, which permits any non-commercial use, sharing, distribution and reproduction in any medium or format, as long as you give appropriate credit to the original author(s) and the source, provide a link to the Creative Commons licence, and indicate if you modified the licensed material. You do not have permission under this licence to share adapted material derived from this article or parts of it. The images or other third party material in this article are included in the article's Creative Commons licence, unless indicated otherwise in a credit line to the material. If material is not included in the article's Creative Commons licence and your intended use is not permitted by statutory regulation or exceeds the permitted use, you will need to obtain permission directly from the copyright holder. To view a copy of this licence, visit <http://creativecommons.org/licenses/by-nc-nd/4.0/>.

© The Author(s) 2025